alkene precursors. Moreover, if a precursor with more than one C=C bond were used, two or more stereogenic centers could be introduced in one step with absolute stereocontrol. Because (*E*)- and (*Z*)-olefins are converted to products of opposite configuration, the relative stereochemistry can be controlled by proper choice of the geometry of the individual C=C bonds.

In this way, to take one example, the stereocenters in the terpenoid side chain of tocopherols could be introduced stereoselectively (Fig. 3), providing an attractive route to these biologically and economically important fat-soluble antioxidants, which are the main components of vitamin E. Despite considerable effort in various laboratories, no commercially viable stereoselective total synthesis of (*RRR*)-tocopherols has been developed so far (*25*).

To demonstrate the potential of our catalysts for transformations of this type, we studied the hydrogenation of γ-tocotrienyl acetate **16** (Fig. 4). In this reaction, which involves hydrogenation of three C=C bonds, two new stereogenic centers are created and, therefore, four stereoisomers can be formed. Because the two prochiral double bonds are both (*E*)-configured, the sense of asymmetric induction at the two reaction sites is expected to be the same, leading either to the (*RR*)- or (*SS*)-configuration depending on the absolute configuration of the catalyst. The influence of the stereogenic center present in the substrate is very weak, as shown by hydrogenation with an achiral iridium catalyst [ligand **2** (R^1 = H, R^2 = Ph); face selectivity, 59:41 and 52:48 at the C(3′) and C(7′) double bond, respectively]. Determination of the isomeric composition of the hydrogenation product is difficult, but a suitable method has been described that involves GC analysis after conversion of the acetate **17** to the corresponding methyl ether (*26*, *27*).

We screened various iridium catalysts derived from ligands of types **2** to **6** (Fig. 1) in the hydrogenation of tocotrienol derivatives (*28*). Whereas oxazoline-based ligands showed disappointingly low stereoselectivities, imidazolines **4** and pyridine-phosphinites **6** gave encouraging results. The most efficient ligand in the imidazoline series was derivative (*R*)-**15**, producing a 90:5:4:1 mixture of (*RRR*)-, (*RRS*)-, (*RSR*)-, and (*RSS*)-tocopheryl acetates (*21*, *22*). However, the best stereoselectivity was achieved with the iridium catalyst derived from pyridine-phosphinite ligand **11**, which gave almost exclusively the natural (*RRR*)-isomer of γ-tocopheryl acetate **17** (*29*), thus providing a highly effective stereoselective route to this important class of bioactive antioxidants. Previously developed strategies for the stereoselective synthesis of vitamin E compounds (*25*) use a stepwise approach for the introduction of the stereogenic centers in the side chain. Here, the natural *RR* configuration is established in a single step.

References and Notes

1. J. M. Brown, in *Comprehensive Asymmetric Catalysis*, E. N. Jacobsen, A. Pfaltz, H. Yamamoto, Eds. (Springer, Berlin, 1999), vol. I, chap. 5.1, pp. 121–182.
2. R. Noyori, *Angew. Chem. Int. Ed. Engl.* **41**, 2008 (2002).
3. W. S. Knowles, *Angew. Chem. Int. Ed. Engl.* **41**, 1998 (2002).
4. H. U. Blaser, E. Schmidt, Eds., *Asymmetric Catalysis on Industrial Scale* (Wiley-VCH, Weinheim, Germany, 2004).
5. A. Lightfoot, P. Schnider, A. Pfaltz, *Angew. Chem. Int. Ed. Engl.* **37**, 2897 (1998).
6. A. Pfaltz *et al.*, *Adv. Synth. Catal.* **345**, 33 (2003).
7. S. P. Smidt, F. Menges, A. Pfaltz, *Org. Lett.* **6**, 2023 (2004).
8. W. J. Drury III *et al.*, *Angew. Chem. Int. Ed. Engl.* **43**, 70 (2004).
9. S. P. Smidt, N. Zimmermann, M. Studer, A. Pfaltz, *Chem. Eur. J.* **10**, 4685 (2004).
10. F. Menges, M. Neuburger, A. Pfaltz, *Org. Lett.* **4**, 4713 (2002).
11. F. Menges, thesis, University of Basel (2004).
12. For related work of other research groups, see (*13–18*); for a review of catalytic homogeneous asymmetric hydrogenations of largely unfunctionalized alkenes, see (*19*).
13. R. D. Broene, S. L. Buchwald, *J. Am. Chem. Soc.* **115**, 12569 (1993).
14. V. P. Conticello *et al.*, *J. Am. Chem. Soc.* **114**, 2761 (1992).
15. T. Bunlaksananusorn, K. Polborn, P. Knochel, *Angew. Chem. Int. Ed. Engl.* **42**, 3941 (2003).
16. Y. Fan, X. Cui, K. Burgess, M. B. Hall, *J. Am. Chem. Soc.* **126**, 16688 (2004).
17. K. Källström, C. Hedberg, P. Brandt, A. Bayer, P. G. Andersson, *J. Am. Chem. Soc.* **126**, 14308 (2004).
18. D. Liu, W. Tang, X. Zhang, *Org. Lett.* **6**, 513 (2004).
19. X. Cui, K. Burgess, *Chem. Rev.* **105**, 3272 (2005).
20. S. Kaiser, thesis, University of Basel (2005).
21. See supporting material on *Science* Online.
22. Catalysts were prepared as previously decribed; hydrogenations were carried out under standard conditions (*5*, *6*).
23. R. L. Danheiser, J. S. Novick, *J. Org. Chem.* **56**, 1176 (1991).
24. C. Wedler, H. Kunath, H. Schick, *J. Org. Chem.* **60**, 758 (1995).
25. T. Netscher, *Chimia (Aarau)* **50**, 563 (1996).
26. N. Cohen *et al.*, *Helv. Chim. Acta* **64**, 1158 (1981).
27. W. Walther, T. Netscher, *Chirality* **8**, 397 (1996).
28. B. Wüstenberg, thesis, University of Basel (2003).
29. In the hydrogenation of the enantiomeric substrate (*S*)-**16**, >98% of (*SRR*)-**17** was obtained with this ligand; this finding confirms that the stereoselectivity is controlled by the catalyst and that the influence of the stereogenic center in the substrate is negligible.
30. The absolute configuration of the products has not yet been determined. The ee values are based on HPLC (product **8**) and GC analysis (**10**) using chiral columns (*21*).
31. Supported by the Swiss National Science Foundation, the Commission for Technology and Innovation (Switzerland), and DSM Nutritional Products.

Plastic Deformation of MgGeO₃ Post-Perovskite at Lower Mantle Pressures

Sébastien Merkel,[1]* Atsushi Kubo,[2] Lowell Miyagi,[1] Sergio Speziale,[1] Thomas S. Duffy,[2] Ho-kwang Mao,[3] Hans-Rudolf Wenk[1]

Polycrystalline MgGeO₃ post-perovskite was plastically deformed in the diamond anvil cell between 104 and 130 gigapascals confining pressure and ambient temperature. In contrast with phenomenological considerations suggesting (010) as a slip plane, lattice planes near (100) became aligned perpendicular to the compression direction, suggesting that slip on (100) or (110) dominated plastic deformation. With the assumption that silicate post-perovskite behaves similarly at lower mantle conditions, a numerical model of seismic anisotropy in the D″ region implies a maximum contribution of post-perovskite to shear wave splitting of 3.7% with an oblique polarization.

The D″ region, the layer above the core-mantle boundary (CMB), exhibits a seismic discontinuity, substantial seismic anisotropy, and considerable lateral heterogeneity, and it plays a key role in our understanding of the deep Earth (*1–4*). Seismic anisotropy in D″ could reflect lattice preferred orientation (LPO) of minerals (*5*) or alignment of structural elements, including layers of melt (*6*, *7*). LPO patterns depend on deformation mechanisms, and interpretation of D″ anisotropy has been ambiguous because of the absence of any experimental constraints on such properties. Here, we report results of an experimental study of deformation of MgGeO₃ post-perovskite (pPv) at high pressures.

Post-perovskite is the stable phase of MgSiO₃ at D″ pressures and is likely to be one of the main constituents of D″ (*8–14*). First-

[1]Department of Earth and Planetary Science, University of California, Berkeley, CA 94720, USA. [2]Department of Geosciences, Princeton University, Princeton, NJ 08544, USA. [3]Geophysical Laboratory, Carnegie Institution of Washington, Washington, DC 20015, USA.

*To whom correspondence should be addressed. E-mail: smerkel@berkeley.edu

principles calculations indicate that it has a strong elastic anisotropy (*9*, *15–17*), and experimental results show that the *b* axis is more compressible than the *a* and *c* axes (*8*). On the basis of structural considerations, pPv has been suggested to form platy crystallites parallel to (010) (fig. S1) or needle-like crystallites in the direction of [100], and (010) has been suggested as the dominant slip plane (*8*, *9*, *15*). In contrast, first-principles calculations indicate that C_{66} is larger than C_{44} and C_{55}, which is incompatible with the concept of a layered structure parallel to (010) (*16*). More recent calculations have also identified a family of polytypes intermediate between Pv and pPv and suggest (110) as a dominant slip plane (*18*).

We deformed a sample of polycrystalline $MgGeO_3$-pPv plastically in the diamond anvil cell between 104 and 130 GPa, heating to 1600 K in different cycles, and observed the evolution of LPO in the sample in situ using radial x-ray diffraction (*19*). Germanates have long been regarded as suitable low-pressure analogs for silicates, based on crystal chemistry systematics and the similarity of slip systems (*20–22*). $MgGeO_3$ exhibits nearly the same transition sequence as $MgSiO_3$ with increasing pressure, including a transition to a pPv phase at about 63 GPa (*23*). $MgGeO_3$-pPv also displays a strong elastic anisotropy (*23*). The transition pressure to the pPv phase in $MgGeO_3$ is almost half that of $MgSiO_3$ (120 GPa), and the diffraction intensity of $MgGeO_3$ is greater than $MgSiO_3$. Therefore, $MgGeO_3$ is a good candidate for experimental investigation of plasticity of pPv phases under deep mantle pressures.

We performed an angle dispersive radial x-ray diffraction experiment (fig. S2) at the High-Pressure Collaborative Access Team (HPCAT) sector of the Advanced Photon Source (beamline 16-ID-B). Starting material was a powder of pure $MgGeO_3$ orthopyroxene mixed with 10 weight percent Pt powder that served as pressure calibrant and laser absorber. It was compressed to a pressure of 104 GPa and then converted into the pPv phase by laser heating in different locations at a temperature of 1600 K for about 10 min. Pressure was then increased to 124 GPa over 5 hours. At this stage, the sample was left for 15 hours to allow relaxation of stresses and strains. Later, the sample was further heated for about 20 min at 1600 K and left for 18 hours to allow relaxation. At the end of this cycle, pressure in the sample was on the order of 130 GPa (table S1). At every step, we collected radial diffraction patterns to evaluate the pressure, stress, and LPO in the sample (*24*).

The diffraction images show substantial variations of diffraction peak positions and intensities with orientation relative to the compression direction (Fig. 1) that can be used to estimate stress and deduce LPO. We analyzed the x-ray diffraction images with two different methods (*24*): One relies on individual peak fitting (*19*), and the other relies on a full image analysis with the Rietveld method (*25*). The differential stress in the $MgGeO_3$-pPv sample ranged from 3.6 to 8.9 GPa and evolved continuously with increasing pressure (table S1). The texture we obtained is represented as inverse pole figures of the compression direction in Fig. 2. We observed a texture with a maximum between (100) and (110) at 104 GPa that did not change with time, further heating, or further compression. At 104 and 130 GPa, the ODF maximums were 1.89 and

1.96 multiples of a random distribution, respectively (table S1). A distinct minimum was at (010). Results from individual peak fitting (Fig. 2B) and the Rietveld method (Fig. 2C) were similar.

To interpret the observed textures, we simulated the development of LPO in pPv polycrystals deformed by slip in compression using a viscoplastic self-consistent (VPSC) polycrystal plasticity model (*26*). The LPO evolution depends on the imposed deformation history and the active slip systems. At this point, little is known about deformation mechanisms in pPv. Therefore, we decided to investigate several combinations of slip systems and critical resolved shear stresses for (100), (010), (001), and (110) (table S2). In agreement with predictions of first-principles calculations suggesting (110) as slip plane in pPv (*18*), the best match with experiments was obtained for simulations with dominant slip on (100), (110), or a combination of the two (Fig. 2, D and G), indicating that those are the most likely slip planes at the conditions of the experiment. Slip on (010) and (001) did not produce a maximum near (100), and slip on (010) produced a maximum rather than the observed minimum at (010) (Fig. 2, E and F). A comparison between the strength of the experimental and calculated textures indicates that the macroscopic compressive strain was 0.2 in the experiment.

There are limitations in using analogs to extract meaningful rheological properties at temperature, stress, and strain rate conditions that are far removed from those in the earth. However, assuming that (100) and (110) slip also applies to $MgSiO_3$-pPv under deep mantle
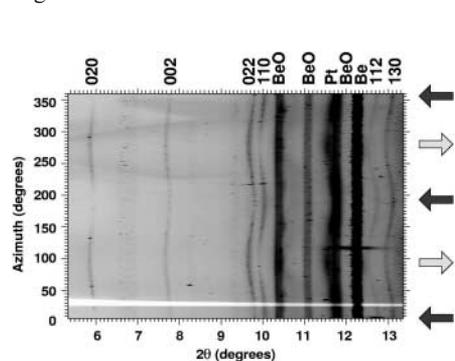
Fig. 1. Unrolled diffraction image of $MgGeO_3$ measured in radial geometry, in situ, at 130 GPa. The directions of maximum and minimum stress are indicated by the black and gray arrows, respectively. LPO and deviatoric stress are deduced from the variations of diffraction intensity and peak position with orientation. Diffraction peaks from the $MgGeO_3$ sample, Pt pressure calibrant, and Be and BeO from the gasket material are labeled on the figure. Because of the geometry of the experiment, Be and BeO peaks always appear as double lines.
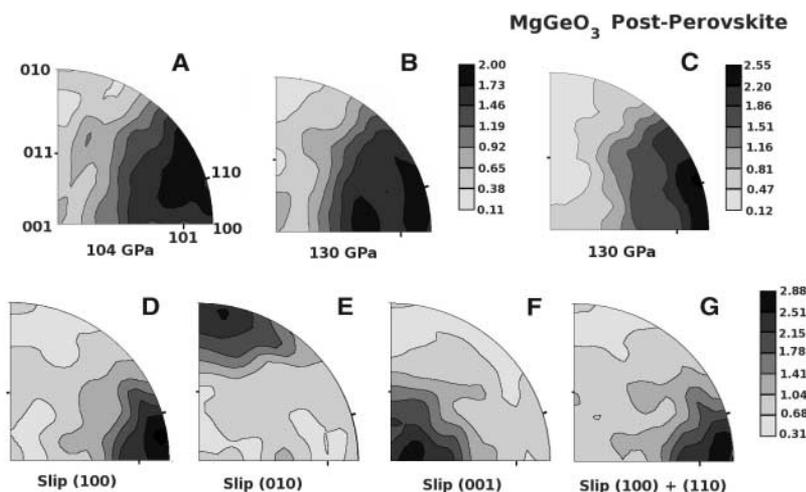
Fig. 2. Inverse pole figure showing the preferred orientation pattern in $MgGeO_3$ pPv in compression measured (**A**) at 104 GPa just after converting the material to the pPv phase; (**B**) at 130 GPa, 41 hours later, after cycles of laser heating and pressure increase, calculated using the individual peak fitting method; (**C**) at 130 GPa, calculated using the Rietveld method; and (**D** to **G**) simulated after 20% compressive strain with models that favor slip along (100), (010), (001), and both (100) and (110), respectively. Equal-area projection is used, and linear contours are expressed in multiples of random distribution.
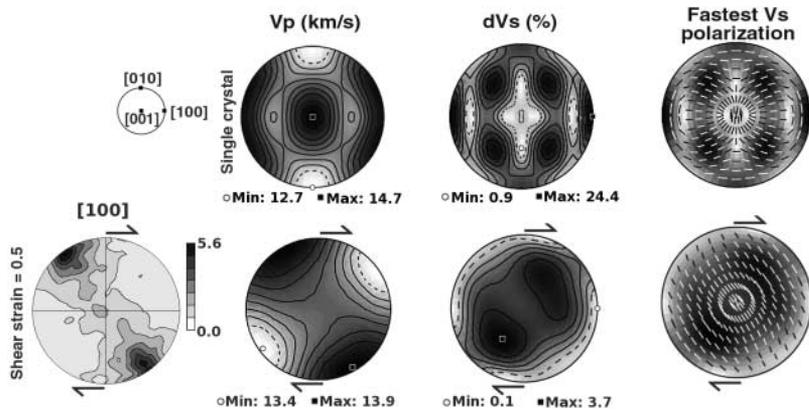
Fig. 3. Modeled three-dimensional compressional velocities (V_P), shear wave splitting (dV_S), and fastest shear wave polarization at 135 GPa and 4000 K for $MgSiO_3$ pPv single crystal (top row) and for a polycrystal aggregate (bottom row) after simple shear plastic deformation up to a strain of 0.5, along with the corresponding [100] pole figure. Linear scale, equal-area projection. Contours for [100], V_P, and dV_S pole figures are expressed in multiples of a random distribution, kilometers per second, and percentage, respectively. Black and white lines (for low and high anisotropy, respectively) in right panel indicate the direction of polarization of the fast shear wave.
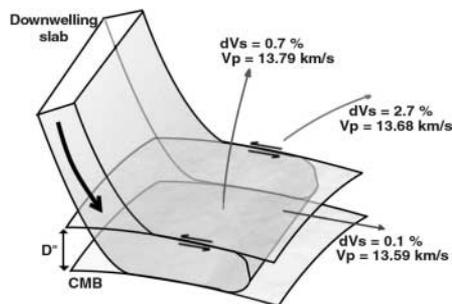
Fig. 4. Contribution of silicate-pPv to anisotropy in a region deformed in simple shear parallel to the CMB.

conditions, we obtained an estimate of expected anisotropies in the D″ layer using again VPSC polycrystal plasticity models to calculate the three-dimensional orientation distribution and then average the single-crystal elastic tensors as a function of crystallographic orientation. From the aggregate elastic tensor, we then calculated seismic velocities in different directions. As a typical deformation path for shear zones, we used simple shear to an equivalent strain of 0.5, corresponding to a shear $\gamma = 0.86$, and slip system combinations that favor slip on (100) and (110). For such a model, the [100] axes tend to align in an oblique maximum rotated from the shear plane normal against the direction of shear (Fig. 3).

The single-crystal anisotropy calculated at 135 GPa and 4000 K (*17*) for *P* waves is 15% (Fig. 3), and shear wave splitting (dV_S) reaches 24%, but the pattern is complex. The polycrystal average for simple shear deformation displays a weak directional anisotropy of only 3.4% for *P* waves and a maximum of 3.7% for shear wave splitting. The relatively low anisotropy is related to the complex single-crystal

elastic tensor where maxima and minima are superposed during averaging. For *S* waves, the largest amount of splitting occurs at an inclination of about 45° from both the plane and direction of shear.

Seismological observations have reported large delays for shear waves that graze horizontally through the D″ region with shear wave splitting delays of up to 10 s, corresponding to a polarization anisotropy of up to 3% in D″. These observations have also shown that the anisotropy style—$V_{SH} > V_{SV}$, $V_{SH} < V_{SV}$ (where V_{SH} and V_{SV} are the velocities of the horizontally and vertically polarized shear waves, respectively), or tilted transverse anisotropy—varies regionally (*2, 4, 27–29*). For a region in which deformation occurs in simple shear parallel to the CMB, we found that the contribution of pPv to shear wave splitting should range from 0.1 to 3.1% for waves traveling in the plane of shear (Fig. 4). In agreement with recent seismic observations of tilted transverse anisotropy in D″ (*28, 29*), we also found that for silicate pPv the polarization anisotropy is usually inclined by about 45° compared with the plane of shear.

These results underline the importance of high-pressure experimentation in assessing plasticity and seismic anisotropy in the deep Earth. In the future, this work will have to be complemented with experiments on silicate pPv itself, higher temperatures, and lower strain rates.

References and Notes

1. M. Wysession *et al.*, in *The Core-Mantle Boundary Region*, M. Gurnis, M. Wysession, E. Knittle, B. Buffet, Eds. (American Geophysical Union, Washington, DC, 1998), pp. 273–297.
2. T. Lay, Q. Williams, E. J. Garnero, *Nature* **392**, 461 (1998).
3. I. Sidorin, M. Gurnis, D. V. Helmberger, *Science* **286**, 1326 (1999).
4. M. Panning, B. Romanowicz, *Science* **303**, 351 (2004).
5. A. K. McNamara, P. E. van Keken, S. I. Karato, *Nature* **416**, 310 (2002).
6. Q. Williams, E. J. Garnero, *Science* **273**, 1528 (1996).
7. J. M. Kendall, in *The Core-Mantle Boundary Region*, M. Gurnis, M. E. Wysession, E. Knittle, B. A. Buffet, Eds. (American Geophysical Union, Washington, DC, 1998), pp. 97–118.
8. M. Murakami, K. Hirose, K. Kawamura, N. Sata, Y. Ohishi, *Science* **304**, 855 (2004).
9. A. R. Oganov, S. Ono, *Nature* **430**, 445 (2004).
10. W. L. Mao *et al.*, *Proc. Nat. Acad. Sci. U.S.A.* **101**, 15867 (2004).
11. S. Shim, T. S. Duffy, R. Jeanloz, G. Shen, *Geophys. Res. Lett.* **31**, L10603 (2004).
12. R. Caracas, R. E. Cohen, *Geophys. Res. Lett.* **32**, L16310 (2005).
13. J. W. Hernlund, C. Thomas, P. J. Tackley, *Nature* **434**, 882 (2005).
14. M. Murakami, K. Hirose, N. Sata, Y. Ohishi, *Geophys. Res. Lett.* **32**, L03304 (2005).
15. T. Iitaka, K. Hirose, K. Kawamura, M. Murakami, *Nature* **430**, 442 (2004).
16. T. Tsuchiya, J. Tsuchiya, K. Umemoto, R. M. Wentzcovitch, *Geophys. Res. Lett.* **31**, L14603 (2004).
17. S. Stackhouse, J. P. Brodholt, J. Wookey, J.-M. Kendall, G. D. Price, *Earth Planet. Sci. Lett.* **230**, 1 (2005).
18. A. R. Oganov, R. Martonák, A. Laio, P. Raiteri, M. Parrinello, *Nature* **438**, 1142 (2005).
19. S. Merkel *et al.*, *J. Geophys. Res.* **107**, 2271 (2002).
20. N. L. Ross, A. Navrotsky, *Am. Mineral.* **73**, 1355 (1988).
21. C. Dupas-Bruzek, T. N. Tingle, H. W. Green II, N. Doukhan, J.-C. Doukhan, *Phys. Chem. Mineral.* **25**, 501 (1998).
22. J. D. Lawlis, Y. H. Zhao, S. I. Karato, *Phys. Chem. Mineral.* **28**, 557 (2001).
23. K. Hirose, K. Kawamura, Y. Ohishi, S. Tateno, N. Sata, *Am. Mineral.* **90**, 262 (2005).
24. Materials and methods are available as supporting material on *Science* Online.
25. H. R. Wenk *et al.*, *Earth Planet. Sci. Lett.* **226**, 507 (2004).
26. H. R. Wenk, in *Texture and Anisotropy*, U. F. Kocks, C. N. Tomé, H. R. Wenk, Eds. (Cambridge University Press, Cambridge, UK, 1998), pp. 560–595.
27. M. Moore, E. J. Garnero, T. Lay, Q. Williams, *J. Geophys. Res.* **109**, B02319 (2004).
28. E. J. Garnero, V. Maupin, T. Lay, M. J. Fouch, *Science* **306**, 259 (2004).
29. J. Wookey, J. M. Kendall, G. Rümpker, *Geophys. J. Int.* **161**, 829 (2005).